CHEMISTRY OF MATERIALS

Article

pubs.acs.org/cm

Explaining Performance-Limiting Mechanisms in Fluorophosphate Na-Ion Battery Cathodes through Inactive Transition-Metal Mixing and First-Principles Mobility Calculations

Ian L. Matts,[†] Stephen Dacek,[†] Tomasz K. Pietrzak,[‡] Rahul Malik,[†] and Gerbrand Ceder*[,†]

[†]Department of Materials Science and Engineering, Massachusetts Institute of Technology, Cambridge, Massachusetts 02139, United States

[‡]Faculty of Physics, Warsaw University of Technology, Koszykowa 75, 00-662, Warsaw, Poland

ABSTRACT: Fluorophosphate cathodes are currently one of the most promising polyanionic sodium-ion battery cathodes and exhibit specific energies not far below oxide cathodes. To further improve fluorophosphate cathodes, their capacity must be increased, which might be possible since some sodium (Na) remains unextracted in these cathodes during cycling. In this study we attempt to answer the question of what specific mechanism limits fluorophosphate cathode capacity, which could stem from either redox-limiting or site-limiting behavior. This paper reports the synthesis, electrochemical characterization, and computational examination of $Na_3GaV(PO_4)_2F_3$. This test system, which was designed explicitly for uncovering the limiting factors in these structures, exhibits reversible insertion of Na^+ and redox activity for V^{2+} through V^{5+} during electrochemical cycling, indicating that fluorophosphate cathodes are not fundamentally redox-limited and must be site-limited. First-principles calculations indicate that large diffusion barriers at high sodiations impose a kinetic limit on Na^+ insertion in fluorophosphate cathodes, but further investigation is needed to determine capacity limits on Na^+ extraction. From our combined results we also propose possible routes to improve future fluorophosphate cathodes.

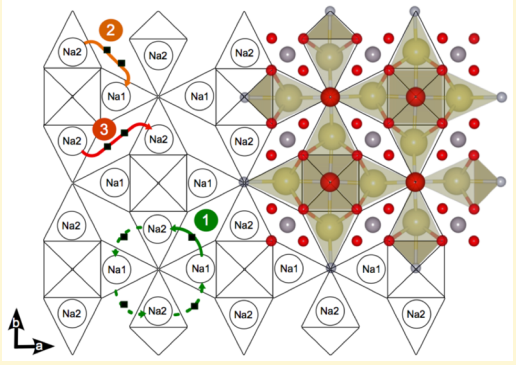

INTRODUCTION

Secondary storage is one of the largest barriers currently preventing the widespread adoption of electric vehicles and renewable sources of energy as a base-load power source in electrical grids. In facing this problem, the current leading technology for energy storage is the lithium-ion (Li-ion) battery. However, the need for increased energy storage coupled with concerns about the cost and availability of metals used in Li-ion battery cathodes has fueled a resurgence in the study of sodium-ion (Na-ion) batteries.[1−4] To date, layered oxide Na-ion battery cathodes have demonstrated the best capacities and energy densities, and as a result they have received the majority of research attention. Despite this, oxide cathodes face significant problems including Na-ion ordering, dramatically stepped voltage plateaus, phase transformations during cycling, and poor cyclability.[5−8]

Polyanionic Na-ion cathodes could prove to be a better choice than oxide cathodes. Polyanionic cathodes constitute a wide design space and offer compositional flexibility when designing new materials with high redox potential. Of the polyanionic Na-ion battery cathodes examined, fluorophosphates are currently the most promising. They have been shown experimentally to exhibit energy densities comparable to the best oxide cathodes, with very high cycling stability.[9,10] $Na_3V_2(PO_4)_2F_3$ is the most studied material of this class, and it has been demonstrated to reversibly cycle at a capacity of around 128 mA·h/g, which is the theoretical capacity of the V^{3+}/V^{4+} redox couple, at an average voltage of ∼3.75 V.[9] Figure 1a shows the electrochemical cycling characteristics of $Na_3V_2(PO_4)_2F_3$ schematically, with composition and capacity on the x axis and the corresponding calculated redox potentials for each regime labeled.

While this is high performance for a polyanionic Na-ion cathode, an energy density of ∼470 W·h/kg would not be enough to supplant Li-ion battery cathodes, or even Na-ion battery oxide cathodes. Consequently, Kang,[11] Rojo,[12] Good-enough,[13] and others have tried to improve upon the performance of these cathodes through oxygen substitution, making cathodes of the type $Na_3V_2O_{2x}(PO_4)_2F_{3-2x}$. Substituting oxygen for fluorine increases the starting valence state of vanadium, which had the potential to increase the performance of oxyfluorophosphate cathodes over fluorophosphate cathodes. Together, in fluorophosphate and oxyfluorophosphate cathodes, both the V^{3+}/V^{4+} and V^{4+}/V^{5+} redox couples have been accessed reversibly and contribute significantly to capacity. So far, no modified fluorophosphate cathodes have significantly exceeded the one-electron capacity (∼130 mA·h/g),[9,11−13] and

Received: June 16, 2015
Revised: August 7, 2015

DOI: 10.1021/acs.chemmater.5b02299
Chem. Mater. XXXX, XXX, XXX−XXX

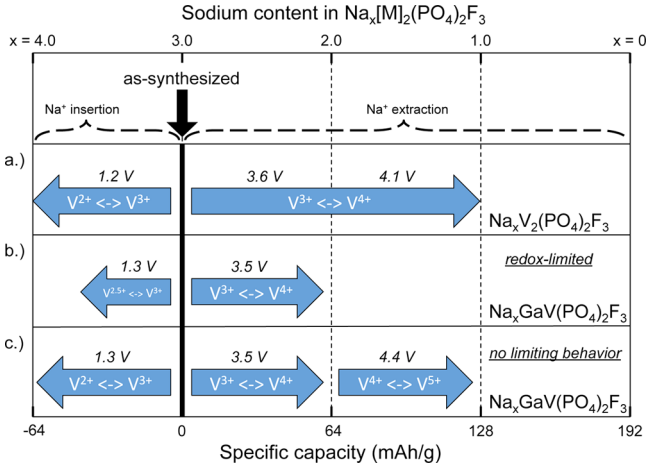

Figure 1. Graphical representation of theoretical redox activity between 1 and 4.5 V for (a) $Na_xV_2(PO_4)_2F_3$ and $Na_xGaV(PO_4)_2F_3$ under the assumptions of (b) redox-limiting and (c) no limiting behavior as a function of Na content. The calculated voltage of each redox reaction is also labeled.

therefore these materials do not significantly improve on the performance of unoxidized $Na_3V_2(PO_4)_2F_3$.

To make fluorophosphate cathodes competitive, the capacity must be substantially improved. The potential exists to achieve capacities as high as 192 mA·h/g, assuming all sodium can be extracted, and up to 256 mA·h/g if sodium can also be inserted to fill all available sites, making $Na_4V_2(PO_4)_2F_3$. Therefore, our goal for this work is to determine the source of the observed limitation of capacity in $Na_3V_2(PO_4)_2F_3$-type cathodes. Specifically, the inability to expand the vanadium redox past one electron per transition-metal ion must be the result of either a limitation in the accessible redox states of vanadium during a single cycle or limitations in moving sodium in and out of the cathode crystal structure. For conciseness, we will refer to these as "redox-limited" and "site-limited" cases for the remainder of this work. Answering this question for $Na_3V_2(PO_4)_2F_3$ is especially complex because as-synthesized $Na_3V_2(PO_4)_2F_3$ has partially occupied Na^+ sites, vanadium can potentially exist in four redox states, and fluorine and phosphate anions tend to lead to relatively insulating phases. As such, improvement strategies might focus on the working ion, transition-metal ions, or anions depending on the source of capacity limitation. For this work we will be focusing on explaining observed capacity limits using mixing of judiciously chosen transition metals.

To pinpoint the source of the observed capacity limit in fluorophosphate cathodes, we used a combined experimental and first-principles calculations approach. First, to decouple the Na concentration from the vanadium redox state and clarify either redox-limited or site-limited behavior, electrochemically inactive Ga^{3+} was incorporated on the vanadium site through the synthesis of $Na_3GaV(PO_4)_2F_3$. This dilution of the active transition metal forces the vanadium redox capability to a wider range, even with small changes in sodium content. From the results of electrochemical characterization, which we will discuss below, we conclude that the origin of capacity limitation is not due to vanadium redox accessibility, which motivates the first-principles investigation of the energetics and mobility associated with Na sites in this crystal structure. From the computational study, we show that the capacity limitation in the discharged limit originates from prohibitively large diffusion barriers in the cathode crystal structure. In the charged limit, however, we observe no kinetic limitation to Na^+ intercalation and surmise that strongly stabilized sodium orderings might be responsible for the capacity constraint. Finally, we offer pragmatic suggestions to overcome these limitations.

EXPERIMENTAL METHODS

Material Synthesis. $Na_3V_2(PO_4)_2F_3$ and $Na_3GaV(PO_4)_2F_3$ samples were made using a standard two-step solid-state synthesis method similar to that previously presented in the literature for fluorophosphate cathodes.[9] To synthesize $Na_3V_2(PO_4)_2F_3$ stoichiometric amounts of V_2O_5 (Alfa Aesar, 99.2%) and $NH_4H_2PO_4$ (Sigma-Aldrich, 99.999%) were mixed with 15% carbon black (Super P) by mass. For $Na_3GaV(PO_4)_2F_3$ the starting mixture composed of stoichiometric amounts of V_2O_5 (Alfa Aesar, 99.2%), Ga_2O_3 (Sigma-Aldrich, >99.99%), and $NH_4H_2PO_4$ (Sigma-Aldrich, 99.999%) was mixed with 15% carbon black (Super P) by mass. For $Na_3V_2(PO_4)_2F_3$, the mixture was pelletized and heated to 750 °C under a flow of argon for 4 h, and for $Na_3GaV(PO_4)_2F_3$ the mixture was pelletized and heated to 850 °C under a flow of argon for 8 h. Both resultant mixtures were then crushed, mixed with a stoichiometric mass of NaF, pelletized, and calcined at 750 °C for 2 h under a flow of argon.

Sample Characterization. Phases present in the synthesized samples were identified by powder X-ray diffraction (XRD). XRD measurements were taken using a Rigaku Miniflex II diffractometer (chromium Kα, λ = 2.2897 Å), Rigaku Corporation, Tokyo) in flat-plate mode, scanning from 15° to 65° 2θ. Lattice parameters in the single-phase polycrystalline sample were determined through diffraction data via Rietveld refinement using HighScore Plus software (PANalytical, The Netherlands) .

The synthesized samples were ball-milled with carbon in a Retsch PM200 planetary ball mill to improve the material's electrochemical performance through decreased particle size and carbon coating.[14,15] The milling was completed in zirconia-lined milling jars that were loaded in a 80:20 mass ratio with active material and carbon (Super P), respectively, in an argon-filled glovebox. The samples were milled for 4 h at 400 rpm, and the resultant powder was unloaded in the Ar-filled glovebox to limit air exposure.

For electrochemical characterization, electrode films were made using a dry-rolling method. Polytetrafluoroethylene (PTFE) binder was added to each ball-milled active material mixture such that the final ratio of components in the prepared electrodes was 76:19:5 by mass, respectively. Each electrode contained approximately 2 mg of active material. Battery cells were made using Swagelok cells with stainless steel current collectors, the dry-rolled cathode films described, glass fiber separator films, a solution of 1 M $NaPF_6$ in ethylene carbonate/diethylene carbonate (1:1) as electrolyte, and a Na metal anode. Galvanostatic experiments were conducted at a rate of C/20 on an Arbin Instruments (College Station, TX) battery cycler.

Computational Methods. All calculations were performed using the Vienna Ab-initio Software Package (VASP) within the projector augmented-wave approach using the Perdew–Burke–Ernzerhof generalized-gradient approximation (GGA) functional and the GGA + U extension.[16−18] A plane-wave energy cut off of 520 eV and a k-point grid of a least 1000 divided by the number of atoms in the unit cell were used for all total energy calculations. All structural relaxations were converged to within 1 meV $atom^{-1}$. A U value of 3.1 eV for vanadum was used in GGA + U calculations for structural relaxations, following the procedure outlined by Jain et al.[19]

We investigated Na^+ migration barriers and vacancy migration barriers using the Nudged Elastic Band (NEB) method, as implemented within the VTST tools package as an extension to VASP.[20,21] In contrast with other total energy calculations, all NEB calculations were performed within the standard GGA (U = 0 eV) functional. We have forgone the + U for NEB calculations due to difficulties converging GGA + U calculations as the result of metastability of electronic states along the Na^+ migration path.[22] In addition, there has been no conclusive evidence showing that GGA + U performs better at predicting cation migration barriers[23−27] despite

DOI: 10.1021/acs.chemmater.5b02299
Chem. Mater. XXXX, XXX, XXX−XXX

improving the accuracy of redox reaction calculations.[28] The diffusion barriers were calculated using a 2 × 2 × 2 gamma-centered k-point grid and with lattice parameters constrained to those of the undefected (GGA) relaxed structures.

Phase diagram and voltage curve construction/analysis was performed using the Python Materials Genomics (pymatgen) library and VASP relaxation calculations were performed using the custodian package.[19,29]

EXPERIMENTAL RESULTS

Synthesis Results. Our $Na_3V_2(PO_4)_2F_3$ synthesis method resulted in a two-phase system consisting of the desired $Na_3V_2(PO_4)_2F_3$ phase with a space group of $P4_2/mnm$ (ICSD powder diffraction file ID 04-012-2207) and an impurity phase of NASICON $Na_3V_2(PO_4)_3$ with the $R\bar{3}c$ space group (ICSD powder diffraction file ID 00-062-0345). While the $Na_3V_2(PO_4)_2F_3$ sample is not a single phase, it is of sufficient purity for use as a qualitative comparison to the compound of primary interest, $Na_3GaV(PO_4)_2F_3$, for this study. $Na_3GaV(PO_4)_2F_3$ was synthesized as a single-phase sample of the desired $P4_2/mnm$ space group. The sharp, nondoublet peaks in the figure indicate that the gallium and vanadium ions in the mixture are not phase-separated. X-ray diffraction spectra for both samples are presented in Figure 2. In addition, experimental vs calculated lattice parameters for $Na_3GaV(PO_4)_2F_3$ are presented in Table 1 and show excellent agreement within the accuracy of what is expected from DFT/PBE + U. The experimental lattice parameters were determined using Rietveld refinement.

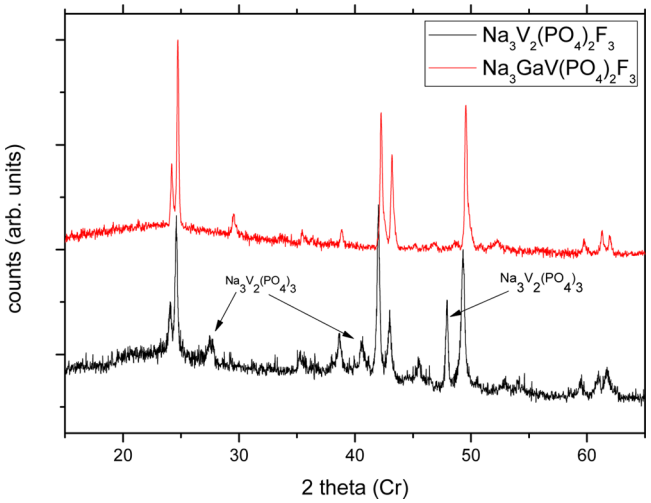

Figure 2. Collected X-ray diffraction spectra for as-synthesized $Na_3V_2(PO_4)_2F_3$ and $Na_3GaV(PO_4)_2F_3$. Impurity peaks are labeled in the spectra.

Electrochemical Characterization Results. Electrochemical cycling curves for $Na_3V_2(PO_4)_2F_3$ and $Na_3GaV(PO_4)_2F_3$ are presented in Figure 3. The data were obtained under galvanostatic conditions at a rate of C/20 in a voltage window of 1.2−4.5 V. In addition, both cycles shown are for the second charge/discharge cycle.

Table 1. Lattice Parameters of $Na_3GaV(PO_4)_2F_3$ from XRD (Rietveld Refinement) and DFT (GGA + U)[a]

		a (Å)	b (Å)	c (Å)	volume (Å^3)
$Na_3GaV(PO_4)_2F_3$	XRD	8.98(9)	8.98(9)	10.70(4)	864.9
	DFT	9.081	9.131	10.805	895.9

[a]DFT error bars for *a*, *b*, *c*, and volume are 1.1%, 2.0%, 1.3%, and 4.3%, respectively.

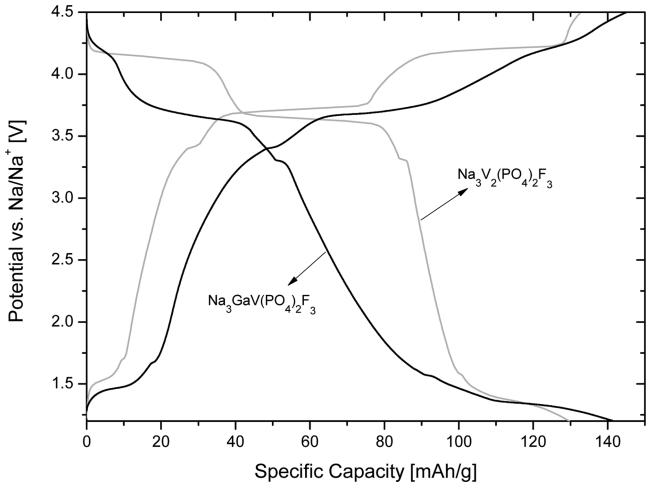

Figure 3. Voltage vs capacity curve for $Na_3GaV(PO_4)_2F_3$ and $Na_3V_2(PO_4)_2F_3$. The second cycle for each compound is shown.

For $Na_3V_2(PO_4)_2F_3$ we observed a charge capacity of 132 mA·h/g and a discharge capacity of 129 mA·h/g, as shown in Figure 3, including the two expected plateaus at 3.6 and 4.2 V, corresponding to activity in the $V^{3+}\leftrightarrow V^{4+}$ redox couple, which is well-documented in the literature.[9,10] In addition, a third plateau is present at 1.5 V on charge and discharge, indicating reversible activity of the $V^{2+} \leftrightarrow V^{3+}$. This indicates reversible Na insertion into the native compound, which has not been previously presented in the literature. Small plateaus at 3.3 and 1.7 V are also observed. This can be attributed to electrochemical activity of $Na_3V_2(PO_4)_3$, an impurity present in the cathode sample, as previously indicated in Figure 2. The observed performance is roughly 80% of that observed in the literature for the voltage window from 2.0 to 4.5 V,[9,10] but this performance is sufficient for our fundamental investigation.

During electrochemical cycling of $Na_3GaV(PO_4)_2F_3$, we observed second cycle charge and discharge capacities of 144 and 141 mA·h/g, respectively. Distinct plateaus are seen in the capacity vs voltage curve at 4.2, 3.7, and 1.4 V, indicating activity of vanadium redox states V^{2+} through V^{5+}. This corresponds well to the calculated voltages for the material from DFT. A calculated voltage vs capacity curve is overlaid on the experimental cycling data of $Na_3GaV(PO_4)_2F_3$ in Figure 4. In the figure, the capacity of the calculated curve is aligned to line up with the portion of the curve corresponding to $V^{3+} \leftrightarrow V^{4+}$ activity. As with the cycling curves for $Na_3V_2(PO_4)_2F_3$, small plateaus are also present in the $Na_3GaV(PO_4)_2F_3$ data at 3.3 and 1.7 V, indicating the likely presence of an electrochemically active $Na_3V_2(PO_4)_3$ impurity. However, no impurity is clear in the XRD spectra shown in Figure 2.

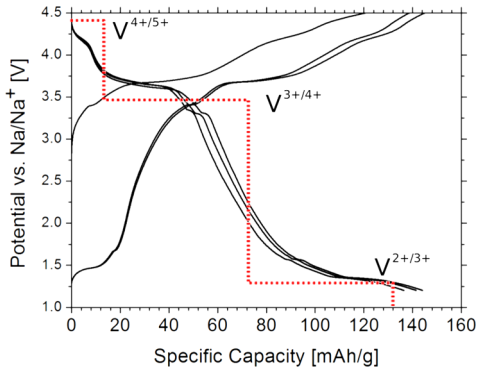

Figure 4. Voltage vs capacity curve for $Na_3GaV(PO_4)_2F_3$. A computed voltage vs capacity curve is overlaid with the predicted redox couples active at each plateau is labeled.

DOI: 10.1021/acs.chemmater.5b02299
Chem. Mater. XXXX, XXX, XXX−XXX

DISCUSSION OF EXPERIMENTAL INVESTIGATION

The observed performance of $Na_3V_2(PO_4)_2F_3$ in this study at voltages between 2.0 and 4.5 V (95 mA·h/g) is around 80% of that observed in the literature.[9,10] Given the unoptimized nature of the cathode, this is acceptable for this study. However, reversible redox activity in $Na_3V_2(PO_4)_2F_3$ below 2 V is a strong indication of reversible insertion of Na^+ ions in the material, indicating activity of the $V^{2+} \leftrightarrow V^{3+}$ redox couple, a phenomenon not yet seen in the existing literature on $Na_3V_2(PO_4)_2F_3$ cathodes. For clarity, we have included Table 2 in which the capacities of the tested materials are separated into extraction and insertion regimes. We take capacity below 2 V to be attributed to electrochemical insertion and capacity above 2 V to be the result of electrochemical extraction of Na ions. The capacity below 2 V is not large for $Na_3V_2(PO_4)_2F_3$, 13 mA·h/g for the second charge and 33 mA·h/g for the second discharge, but given the low voltage capacities' reversibility, we believe this to be a conclusive result that Na^+ can be inserted into the structure.

Table 2. Observed Capacities of $Na_3V_2(PO_4)_2F_3$ and $Na_3GaV(PO_4)_2F_3$ Separated into the Individual Contributions of Electrochemical Na-Ion Insertion (1.2−2.0 V) and Extraction (2.0−4.5 V) for the Second Cycle of Each Compound

compound	half cycle	capacity (1.2−2.0 V)	capacity (2.0−4.5 V)
$Na_3V_2(PO_4)F_3$	charge	13 mA·h/g	119 mA·h/g
	discharge	33 mA·h/g	96 mA·h/g
$Na_3GaV(PO_4)F_3$	charge	22 mA·h/g	122 mA·h/g
	discharge	64 mA·h/g	77 mA·h/g

For $Na_3GaV(PO_4)_2F_3$, our strategy was to use an inactive 3+ dopant to test full range of possible vanadium redox while keeping the Na^+ extraction amount within known bounds, and in doing so deconvolute Na^+ extraction limitations from redox limitations in fluorophosphate cathodes. If it is possible to fully access vanadium redox states between V^{2+} and V^{5+}, and without other major limitations, the cathode would cycle between $Na_4GaV(PO_4)_2F_3$ and $NaGaV(PO_4)_2F_3$, yielding a capacity of 186 mA·h/g. The electrochemical performance for this case is shown schematically in Figure 1c. Conversely, if vanadium is fully redox-limited in this structure, that is, if the amount of extractable Na^+ per vanadium ion is fixed and equal to that observed in $Na_3V_2(PO_4)_2F_3$, the capacity would be halved, leading to an observed capacity of ∼90 mA·h/g upon electrochemical cycling, as shown schematically in Figure 1b. Additionally, in the case of $Na_3GaV(PO_4)_2F_3$, a greater portion of the observed capacity lies below 2 V, which we deem to be voltages at which electrochemical insertion is occurring. Figure 4 shows the first three complete electrochemical cycles for $Na_3GaV(PO_4)_2F_3$, and as such shows good reversibility for the material, particularly for the insertion regime in which the $V^{2+} \leftrightarrow V^{3+}$ redox couple is active. In addition, Figure 4 has a calculated voltage curve overlaid including all three redox couples of vanadium in the mixed transition-metal compound. The curve agrees well with the experimental data, giving further support to the idea that $Na_3GaV(PO_4)_2F_3$ is capable of reversible Na^+ insertion at voltages below 2 V.

During the electrochemical cycling of $Na_3GaV(PO_4)_2F_3$ above 4 V, we observe a small reversible voltage plateau. The capacity observed between 2 and 4 V corresponds well to the theoretical capacity and calculated voltage of the V^{3+}/V^{4+} redox couple in $Na_3GaV(PO_4)_2F_3$, so at 4 V, all of the vanadium would be oxidized to its V^{4+} state from the native compound. Thus, this plateau can not correspond to V^{3+}/V^{4+} activity, and by extension we can infer that it must come from activity in the V^{4+}/V^{5+} redox couple, even though we have not observed the vanadium valence state directly. Combined, the observed voltage curve is consistent with the occurrence of V^{2+}, V^{3+}, V^{4+}, and V^{5+} on a single charge or discharge. The reversible capacity implies electrochemical cycling between a Na content of approximately $Na_{1.8}GaV(PO_4)_2F_3 \leftrightarrow Na_{3.5}GaV(PO_4)_2F_3$. This capacity of 141 mA·h/g significantly exceeds 90 mA·h/g, which is the "redox-limited" case described previously in Figure 1. As a result, $Na_3GaV(PO_4)_2F_3$, and by extension $Na_3V_2(PO_4)_2F_3$, is not fundamentally limited by the redox activity of vanadium. However, the discharge capacity of 141 mA·h/g falls short of the "unlimited" case, also outlined in Figure 1. Therefore, $Na_3GaV(PO_4)_2F_3$ must be site-limited.

COMPUTATIONAL RESULTS

By synthesis and electrochemical characterization of the $Na_3GaV(PO_4)_2F_3$ system, the source of observed capacity limitation in the $Na_3V_2(PO_4)_2F_3$ system can be attributed to a limitation in the Na^+ intercalation process rather than a limit in transition-metal oxidation/reduction. Such site-limited performance is rooted in the material's thermodynamics and/or kinetics due to the energetic relationships of available Na sites and the migration barriers between them, and can be manifested in concentration-dependent diffusivity. From Galvanostatic Intermittent Titration Technique (GITT) experiments performed by Liu et al., the Na chemical diffusivity is observed at its highest ($D_{Na} \approx 10^{-6.2}$ cm^2/s) at $x_{Na} = 1.6$ with drops in the diffusivity at both increasing and decreasing concentrations ($D_{Na} \approx 10^{-7.2}$ cm^2/s at $x_{Na} = 2.7$ and $D_{Na} \approx 10^{-8}$ cm^2/s at $x_{Na} = 1$).[30] To isolate the physical origin for the variation in Na diffusivity, we have performed first-principles mobility calculations in the dilute Na and dilute Na vacancy concentration limits (i.e., $x_{Na} = 0$ and $x_{Na} = 4$).

Two-dimensional Na diffusion occurs within $a-b$ planes ($z = 0$) of the idealized $Na_3V_2(PO_4)_2F_3$ structure as shown in Figure 5a, superimposed above a schematic drawing of the Na layer. In this structure, Na ions (yellow) are encapsulated within 6 + 1 prismatic polyhedra composed of 3 fluorine atoms (blue) and 4 oxygen atoms (red). For clarity, phosphorus atoms (purple), which lie above and below (±0.25) the $z = 0$ plane, are shown and the $V_2(PO_4)_2F_3$ bioctahedra are omitted. Within Figure 5a, the three symmetrically distinct Na sites are shown: The Na1 sites are aligned such that the prismatic site's bisector in the $a-b$ plane is parallel to the a axis, Na2 sites with the prismatic site's bisector is aligned along the b axis, and the Na3 sites (denoted by black squares in Figure 5a) bridge the Na1 and Na2 sites.[31] In the idealized crystal structure, there are three distinct diffusion paths, shown in Figure 5a. Path 1 captures the motion between a Na1 and a Na2 site, passing through the adjoining Na3 site. Path 2 captures the motion between a Na1 and a Na2 site passing through two adjoining Na3 sites. Path 3 captures the motion between neighboring Na2 sites and requires diffusion through two Na3 sites. Under symmetry of this material in the fully sodiated and desodiated limits, the diffusion between neighboring Na1 sites is also described by path 3.

In Figure 5b,c the migration energies corresponding to paths 1, 2, and 3 in the $Na_3V_2(PO_4)_2F_3$ structure are shown in green, orange, and red, respectively, against their normalized path lengths in the fully sodiated (dashed) and desodiated limits (solid). In both limits, path 1 barriers are much lower (∼20−45 meV) than the path 2 (∼300−600 meV) and path 3 (∼300−1100 meV) barriers. The shape of the migration energy for path 1 in Figure 5b can be understood by considering the idealized trajectory highlighted in Figure 5a in green, as the local minimum observed halfway through the diffusion path corresponds to the Na3 site. Although the path 1 barrier's shape is

DOI: 10.1021/acs.chemmater.5b02299
Chem. Mater. XXXX, XXX, XXX−XXX

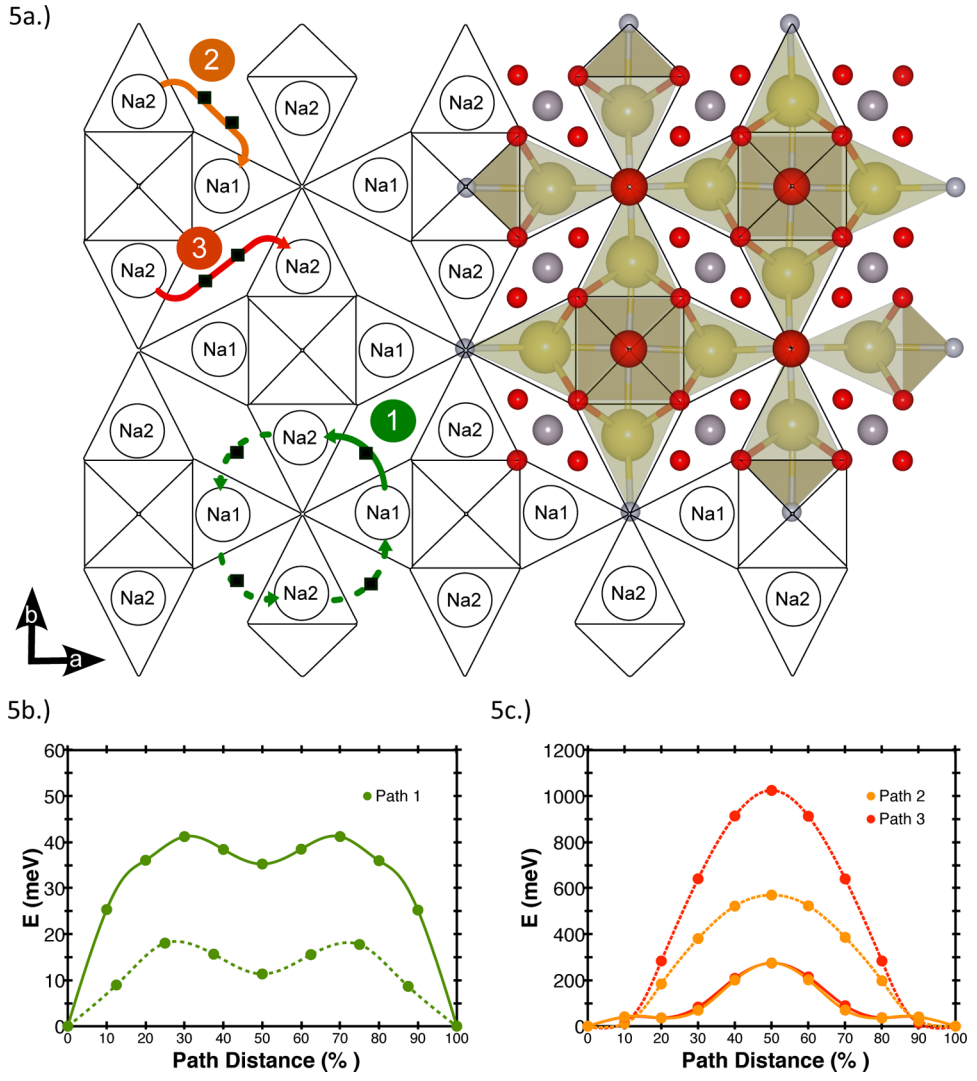

Figure 5. (a) A schematic image of the $Na_xV_2(PO_4)_2F_3$ crystal structure in a Na (z = 0) plane. Na1 and Na2 Na sites are marked and filled as would be expected in the fully occupied $Na_4V_2(PO_4)_2F_3$ crystal structure. A structure image with yellow 6 + 1 coordinated, capped prismatic Na sites is shown, overlaid for clarification. Idealized diffusion paths are drawn and labeled 1, 2, and 3. Black squares are drawn within these paths to demonstrate diffusion through sixfold coordinated prismatic Na3 sites. Path 1 is repeated to demonstrate the ring pattern associated with consecutive path 1 jumps. (b) Diffusion barriers for path 1 in the sodiated (dotted) and desodiated (solid) limits. (c) The diffusion barriers for path 2 (orange) and path 3 (red) in the sodiated (dotted) and desodiated (solid) limits.

relatively unchanged in the sodiated limit, the path 2 and path 3 barriers (solid red and orange lines in Figure 5c) change significantly. In the desodiated limit, the path 2 and path 3 migration energies overlap, consistent with the fact that they become identical under the symmetry of the desodiated state. Both trajectories pass through two Na3 sites, which correspond to the subtle dips in the migration energy observed at ∼20% and ∼80% of the path length, and the activated state in between corresponds to crossing the shared face between the two prismatic Na3 sites. In the sodiated limit, however, the path 2 and path 3 barriers both increase (dashed lines in Figure 5c), but by different amounts, which can be rationalized by considering the additional electrostatic interaction of nearby Na^+. For path 2, the electrostatic repulsion of the nearest two Na^+ results increases the energy of the activated state and also alters the trajectory of the migrating Na^+ which performs a "tighter turn" to the adjacent Na site. For path 3, however, the two nearest Na are on opposite sides of the diffusion trajectory, so the readjustment of the path as observed for path 2 is no longer possible. Consequently, the migration barrier for path 3 is significantly higher in the fully sodiated limit.

DISCUSSION OF COMPUTATIONAL STUDY

If Na^+ intercalation were to proceed exclusively through path 1 hops, then by our calculations, we would expect the diffusivity to be 4−5 orders of magnitude greater than the observed values.[30] For reference, assuming a random walk model of diffusion, a migration barrier of ∼300 meV roughly corresponds to a diffusivity of 10^{-9} cm^2/s at room temperature (given an atomic jump frequency $\nu = k_BT/h = 6.2 \times 10^{12}$ s^{-1} and a jump distance a of ∼3 Å), and an increase of 60 meV in the migration barrier corresponds to a decrease in the diffusivity by an order of magnitude. However, by virtue of the $Na_3V_2(PO_4)_2F_3$ crystal topology, the Na sites do not percolate without path 2 or path 3 hops. In other words, Na ions would be restricted to performing circular "laps" fixed in space as depicted by the dashed green arrows forming a circle in Figure 5a and do not contribute to net mean-squared displacement.

The frequency of path 2 and path 3 hops then determine the diffusivity, which we estimate using a simple random walk model. At every Na1 or Na2 site there are two of each possible

DOI: 10.1021/acs.chemmater.5b02299
Chem. Mater. XXXX, XXX, XXX−XXX

diffusion pathway (path 1, path 2, or path 3) available. Since the energy barrier for path 1 migration is the lowest it occurs the most often, lowering the frequency of diffusion along paths that contribute to the mean squared displacement, which are paths 2 and 3, and leading to locally correlated diffusion. The diffusion behavior in the fully sodiated and desodiated limits can be therefore reduced to a two-dimensional random walk with the jump frequency related to the residence time of a Na ion (or vacancy) in the fast diffusing rings depicted in Figure 5a in green and the jump length equal to the distance between ring centers (6.3 Å). The larger the discrepancy in the migration barrier between fast path 1 hops and slower path 2 and path 3 hops, the larger the Na residence time and therefore slower diffusion. From statistical mechanics, the probability p_1 that a Na^+ moves from a Na1 site through a single Na3 site to a Na2 site, or a path 1 hop in Figure 5, is given by

$$p_1 = \frac{\exp(-E_1/\mathrm{kT})}{\exp(-E_1/\mathrm{kT}) + \exp(-E_2/\mathrm{kT}) + \exp(-E_3/\mathrm{kT})} \quad (1)$$

where E_1, E_2, and E_3 are the corresponding migration barriers shown in Figure 5b,c. The average number of path 1 hops before a single path 2 or path 3 hop occurs is then $1/(1 - p_1)$ which is 2.14×10^9 in the sodiated limit (4.49×10^3 in the desodiated limit). From this probability we can approximate the diffusivity in the Na layer as

$$D_{2D} \approx \frac{a^2}{4t_{res}} \quad (2)$$

where a is the distance between ring centers (6.4 Å in the sodiated limit and 6.3 Å in the desodiated limit) and t_{res} is the residency time of a Na atom (or Na vacancy) within an individual ring, defined as

$$t_{res} = \frac{\langle t \rangle}{(1 - p_1)} = \frac{1}{\Gamma}\frac{1}{(1 - p_1)} = \frac{1}{2\nu \exp(-E_1/\mathrm{kT}) + 2\nu \exp(-E_2/\mathrm{kT})} \quad (3)$$

where $\langle t \rangle = 1/\Gamma$ is the mean time for any hop, $\nu = 6.2 \times 10^{12}$ s^{-1} is the assumed atomic jump frequency, and $\Gamma = \sum_i \Gamma_i$ where

$$\Gamma_i = N_i \nu \exp(E_i/\mathrm{kT}) \quad (4)$$

for each barrier E_i and path multiplicity N_i. From this, the reported barriers correspond to calculated diffusivities of the order 4.7×10^{-13} and 8.9×10^{-8} cm^2/s in the fully sodiated ($x_{Na} = 4$) and desodiated ($x_{Na} = 0$) limits, respectively.

The large variation between the calculated diffusivities from the fully charged to discharged limit arises from an increase in the migration barriers for path 2 (E_2) and path 3 (E_3), from ~300 to 600 meV and ~300 to 1000 meV, respectively. The dependence of the local Na occupation on the path 2 and path 3 barriers strongly suggests that Na^+ diffusion proceeds preferentially through a divacancy mechanism, which would result in a decrease in the Na^+ diffusivity with increasing Na^+ intercalation due to the reduced concentration of mobile carriers (divacancies), a phenomenon well-known in the Li_xCoO_2 system as extensively characterized by Van der Ven et al.[32] Indeed, the existence of a preferred divacancy mechanism agrees with the general trend of increasing diffusivity upon charge that has been observed by Liu et al. from $x_{Na} = 3$ to $x_{Na} = 1.6$.[30] The abrupt drop in diffusivity that is observed at $x_{Na} < 1.6$ by Liu et al., however, can not be explained by the divacancy mechanism. Moreover, our mobility calculations suggest that there is no inherent kinetic limitation to accessible capacity in the low Na concentration regime.

Although we determine that the apparent capacity limitation in the charged limit is not purely kinetic in origin, we postulate that the capacity limitation is then thermodynamic in origin, specifically the result of strong Na^+ orderings at intermediate Na concentrations. If there is a Na^+ ordering strongly stabilized at a given composition, then further intercalation requires not only overcoming the Na^+ migration barrier but also the additional energy to disrupt the ordering, either by formation of a vacancy during charge or the incorporation of Na^+ during discharge. Effectively, strong ordering interactions between intercalating species appear as regions of high slope in the open-circuit potential, decrease the concentration of mobile carriers, and accordingly reduce the diffusivity. The contribution of orderings to the diffusivity is formally captured in the so-called "thermodynamic factor" in Fick's second law, and has been investigated in detail for the lithium-ion battery cathode material $LiCoO_2$ by Van der Ven et al.[32] who demonstrate that strong orderings at $x_{Li} = 0.5$ and $x_{Li} = 0.33$ cause sudden, sharp, drops in the diffusivity. In the computed $Na_3V_2(PO_4)_2F_3$ voltage curve shown in Figure 6, there are noticeable steps in the voltage at $x_{Na} = 1$ and $x_{Na} = 3$, suggesting the specific concentrations where one would expect abrupt decreases in the Na^+ diffusivity. Indeed, in the diffusivity measurements performed by Liu et al., the lowest values are measured as these concentrations are approached.[30] The concentration dependence of the diffusivity as measured by Liu et al. is also asymmetric, with a more gradual increase in the diffusivity upon charge until $x_{Na} = 1.6$ followed by a sharp decline at lower concentrations. We attribute this to the added contribution of divacancy limited mobility that has greater effect with increasing discharge, and smears out the more sharp effect on the diffusivity caused by the thermodynamic factor. In the

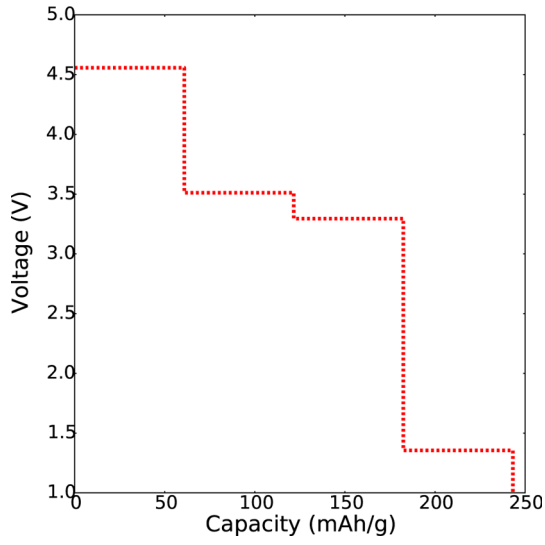

Figure 6. Theoretical voltage vs capacity curve for $Na_3V_2(PO_4)_2F_3$ between compositions of $V_2(PO_4)_2F_3$, at left, and $Na_4V_2(PO_4)_2F_3$, at right.

DOI: 10.1021/acs.chemmater.5b02299
Chem. Mater. XXXX, XXX, XXX−XXX

charged limit, the Na^+ mobility is no longer limited by the concentration of divacancies, resulting in the more pronounced effect of strong Na^+ ordering.

Given the results of the study, we have isolated some of the specific physical mechanisms responsible for the observed capacity limitation in $Na_3V_2(PO_4)_2F_3$ electrodes. Using this clearer understanding, we can propose targeted strategies to further improve performance in fluorophosphate cathodes for Na-ion batteries. Given the limitation in Na^+ mobility in the discharged limit due to the limited concentration of mobile divacancies, significant improvement of the insertion capacity is unlikely. However, we believe there is an opportunity to improve the accessible capacity at the current charged limit, $NaV_2(PO_4)_2F_3$, which has the benefit of being at high voltages (>4 V) and could therefore significantly add to the energy density of these materials. To achieve this, we propose the most promising strategy is to disrupt existing ordering interactions in the Na sublattice by incorporating atomic substitutions in either the Na or vanadium sublattices. This strategy has been successfully employed by Li et al.[33] in Na-ion battery layered oxide cathodes to suppress phase transitions in $NaMn_{1/4}Fe_{1/4}Ni_{1/4}Co_{1/4}O_2$.

CONCLUSION

To investigate the specific physical origin of the capacity limitation of $Na_3V_2(PO_4)_2F_3$ Na-ion battery cathodes, we have performed a systematic experimental and theoretical study to isolate the factors that limit capacity to around its one-electron capacity of 128 mA·h/g. To decouple potential limitations from the Na concentration from those of the vanadium redox state, we have mixed V^{3+} with electrochemically inactive Ga^{3+}, yielding $Na_3GaV(PO_4)_2F_3$. Electrochemical cycling of $Na_3GaV(PO_4)_2F_3$ between 1.2 and 4.5 V yielded a discharge capacity of 141 mA·h/g, with distinct voltage plateaus at 1.5, 3.6, and 4.2 V. On the basis of this, we inferred that V^{2+}, V^{3+}, V^{4+}, and V^{5+} redox states were all accessible during cycling and concluded that the capacity of $Na_3GaV(PO_4)_2F_3$ is not redox-limited and therefore must be site-limited. Ab initio computation was employed to gain further insight, and NEB calculations of diffusion barriers showed that high diffusion barriers during Na^+ insertion prohibit significant capacity in the low-voltage regime at reasonable rates. However, high barriers to Na^+ can not explain the limit at the top of charge, which leads us to believe Na^+ ordering interactions must be the reason for observed capacity limits. From these results, we suspect that improvements in fluorophosphate cathodes may be possible if these orderings can be disrupted through atomic substitutions.

AUTHOR INFORMATION

Corresponding Author

*E-mail: gceder@mit.edu.

Notes

The authors declare no competing financial interest.

ACKNOWLEDGMENTS

The authors thank the Samsung Advanced Institute of Technology for funding this research. Tomasz Pietrzak is grateful to the Center of Advanced Studies at Warsaw University of Technology for being granted funding of the European Union in the framework of European Social Fund through the WUT Development Program. This work was also done in part using the shared facilities in the Center for Materials Science and Engineering (CMSE) at MIT.

REFERENCES

(1) Palomares, V.; Serras, P.; Villaluenga, I.; Hueso, K. B.; Carretero-González, J.; Rojo, T. Na-Ion Batteries, Recent Advances and Present Challenges to Become Low Cost Energy Storage Systems. *Energy Environ. Sci.* **2012**, *5*, 5884−5901.

(2) Kim, S.-W.; Seo, D.-H.; Ma, X.; Ceder, G.; Kang, K. Electrode Materials for Rechargeable Sodium-Ion Batteries: Potential Alternatives to Current Lithium-Ion Batteries. *Adv. Energy Mater.* **2012**, *2*, 710−721.

(3) Slater, M. D.; Kim, D.; Lee, E.; Johnson, C. S. Sodium-Ion Batteries. *Adv. Funct. Mater.* **2013**, *23*, 947−958.

(4) Ellis, B. L.; Nazar, L. F. Sodium and Sodium-Ion Energy Storage Batteries. *Curr. Opin. Solid State Mater. Sci.* **2012**, *16*, 168−177.

(5) Ma, X.; Chen, H.; Ceder, G. Electrochemical Properties of Monoclinic $NaMnO_2$. *J. Electrochem. Soc.* **2011**, *158*, A1307−A1312.

(6) Yabuuchi, N.; Kajiyama, M.; Iwatate, J.; Nishikawa, H.; Hitomi, S.; Okuyama, R.; Usui, R.; Yamada, Y.; Komaba, S. P2-Type $Na_x[Fe_{1/2}Mn_{1/2}]O_2$ Made From Earth-Abundant Elements for Rechargeable Na Batteries. *Nat. Mater.* **2012**, *11*, 512−517.

(7) Didier, C.; Guignard, M.; Denage, C.; Szajwaj, O.; Ito, S.; Saadoune, I.; Darriet, J.; Delmas, C. Electrochemical Na-Deintercalation from $NaVO_2$. *Electrochem. Solid-State Lett.* **2011**, *14*, A75−A78.

(8) Kim, D.; Lee, E.; Slater, M.; Lu, W.; Rood, S.; Johnson, C. S. Layered $Na[Ni_{1/3}Fe_{1/3}Mn_{1/3}]O_2$ Cathodes for Na-Ion Battery Application. *Electrochem. Commun.* **2012**, *18*, 66−69.

(9) Shakoor, R. A.; Seo, D.-H.; Kim, H.; Park, Y.-U.; Kim, J.; Kim, S.-W.; Gwon, H.; Lee, S.; Kang, K. A Combined First Principles and Experimental Study on $Na_3V_2(PO_4)_2F_3$ for Rechargeable Na Batteries. *J. Mater. Chem.* **2012**, *22*, 20535−20541.

(10) Chihara, K.; Kitajou, A.; Gocheva, I. D.; Okada, S.; Yamaki, J. Cathode Properties of $Na_3M_2(PO_4)_2F_3$ [M = Ti, Fe, V] for Sodium-Ion Batteries. *J. Power Sources* **2013**, *227*, 80−85.

(11) Park, Y.-U.; Seo, D.-H.; Kwon, H.-S.; Kim, B.; Kim, J.; Kim, H.; Kim, I.; Yoo, H.-I.; Kang, K. A New High-Energy Cathode for a Na-Ion Battery with Ultrahigh Stability. *J. Am. Chem. Soc.* **2013**, *135*, 13870−13878. PMID: 23952799.

(12) Serras, P.; Palomares, V.; Goni, A.; Gil de Muro, I.; Kubiak, P.; Lezama, L.; Rojo, T. High Voltage Cathode Materials for Na-ion Batteries of General Formula $Na_3V_2O_{2x}(PO_4)_2F_{3-2x}$. *J. Mater. Chem.* **2012**, *22*, 22301−22308.

(13) Xu, M.; Wang, L.; Zhao, X.; Song, J.; Xie, H.; Lu, Y.; Goodenough, J. B. $Na_3V_2O_2(PO_4)_2F$/Graphene Sandwich Structure for High-Performance Cathode of a Sodium-Ion Battery. *Phys. Chem. Chem. Phys.* **2013**, *15*, 13032−13037.

(14) Huang, H.; Yin, S.-C.; Nazar, L. F. Approaching Theoretical Capacity of $LiFePO_4$ at Room Temperature at High Rates. *Electrochem. Solid-State Lett.* **2001**, *4*, A170−A172.

(15) Mi, C. H.; Zhao, X. B.; Cao, G. S.; Tu, J. P. In Situ Synthesis and Properties of Carbon-Coated $LiFePO_4$ as Li-Ion Battery Cathodes. *J. Electrochem. Soc.* **2005**, *152*, A483−A487.

(16) Blöchl, P. E. Projector Augmented-Wave Method. *Phys. Rev. B: Condens. Matter Mater. Phys.* **1994**, *50*, 17953−17979.

(17) Kresse, G.; Furthmüller, J. Efficient Iterative Schemes for Ab Initio Total-Energy Calculations Using a Plane-Wave Basis Set. *Phys. Rev. B: Condens. Matter Mater. Phys.* **1996**, *54*, 11169−11186.

(18) Perdew, J. P.; Burke, K.; Ernzerhof, M. Generalized Gradient Approximation Made Simple. *Phys. Rev. Lett.* **1996**, *77*, 3865−3868.

(19) Jain, A.; Hautier, G.; Moore, C. J.; Ong, S. P.; Fischer, C. C.; Mueller, T.; Persson, K. A.; Ceder, G. A High-Throughput Infrastructure for Density Functional Theory Calculations. *Comput. Mater. Sci.* **2011**, *50*, 2295−2310.

(20) Henkelman, G.; Uberuaga, B. P.; Jonsson, H. A Climbing Image Nudged Elastic Band Method for Finding Saddle Points and Minimum Energy Paths. *J. Chem. Phys.* **2000**, *113*, 9901−9904.

DOI: 10.1021/acs.chemmater.5b02299
Chem. Mater. XXXX, XXX, XXX−XXX

(21) Henkelman, G.; Jónsson, H. Improved Tangent Estimate in the Nudged Elastic Band Method for Finding Minimum Energy Paths and Saddle Points. *J. Chem. Phys.* **2000**, *113*, 9978−9985.
(22) Liu, M.; Rong, Z.; Malik, R.; Canepa, P.; Jain, A.; Ceder, G.; Persson, K. A. Spinel Compounds as Multivalent Battery Cathodes: A Systematic Evaluation Based on Ab Initio Calculations. *Energy Environ. Sci.* **2015**, *8*, 964−974.
(23) Ong, S. P.; Chevrier, V. L.; Hautier, G.; Jain, A.; Moore, C.; Kim, S.; Ma, X.; Ceder, G. Voltage, Stability and Diffusion Barrier Differences Between Sodium-Ion and Lithium-Ion Intercalation Materials. *Energy Environ. Sci.* **2011**, *4*, 3680−3688.
(24) Dathar, G. K. P.; Sheppard, D.; Stevenson, K. J.; Henkelman, G. Calculations of Li-Ion Diffusion in Olivine Phosphates. *Chem. Mater.* **2011**, *23*, 4032−4037.
(25) Lin, H.; Wen, Y.; Zhang, C.; Zhang, L.; Huang, Y.; Shan, B.; Chen, R. A GGA+U Study of Lithium Diffusion in Vanadium Doped $LiFePO_4$. *Solid State Commun.* **2012**, *152*, 999−1003.
(26) Xu, B.; Meng, S. Factors Affecting Li Mobility in Spinel $LiMn_2O_4$−A First-Principles Study by GGA and GGA+U Methods. *J. Power Sources* **2010**, *195*, 4971−4976.
(27) Morgan, D.; van der Ven, A.; Ceder, G. Li Conductivity in Li_xMPO_4 (M = Mn, Fe, Co, Ni) Olivine Materials. *Electrochem. Solid-State Lett.* **2004**, *7*, A30−A32.
(28) Zhou, F.; Cococcioni, M.; Marianetti, C. A.; Morgan, D.; Ceder, G. First-Principles Prediction of Redox Potentials in Transition-Metal Compounds with LDA+ U. *Phys. Rev. B: Condens. Matter Mater. Phys.* **2004**, *70*, 235121.
(29) Ong, S. P.; Richards, W. D.; Jain, A.; Hautier, G.; Kocher, M.; Cholia, S.; Gunter, D.; Chevrier, V. L.; Persson, K. A.; Ceder, G. Python Materials Genomics (Pymatgen): A Robust, Open-Source Python Library for Materials Analysis. *Comput. Mater. Sci.* **2013**, *68*, 314−319.
(30) Liu, Z.; Hu, Y.-Y.; Dunstan, M. T.; Huo, H.; Hao, X.; Zou, H.; Zhong, G.; Yang, Y.; Grey, C. P. Local Structure and Dynamics in the Na-Ion Battery Positive Electrode Material $Na_3V_2(PO_4)_2F_3$. *Chem. Mater.* **2014**, *26*, 2513−2521.
(31) Bianchini, M.; Brisset, N.; Fauth, F.; Weill, F.; Elkaim, E.; Suard, E.; Masquelier, C.; Croguennec, L. $Na_3V_2(PO_4)_2F_3$ Revisited: A High-Resolution Diffraction Study. *Chem. Mater.* **2014**, *26*, 4238−4247.
(32) van der Ven, A.; Ceder, G. Lithium Diffusion in Layered Li_xCoO_2. *Electrochem. Solid-State Lett.* **2000**, *3*, 301−304.
(33) Li, X.; Wu, D.; Zhou, Y.-N.; Liu, L.; Yang, X.-Q.; Ceder, G. O3-Type $Na(Mn_{0.25}Fe_{0.25}Co_{0.25}Ni_{0.25})O_2$: A Quaternary Layered Cathode Compound for Rechargeable Na-ion Batteries. *Electrochem. Commun.* **2014**, *49*, 51−54.

DOI: 10.1021/acs.chemmater.5b02299
Chem. Mater. XXXX, XXX, XXX−XXX